Available online at www.sciencedirect.com
SCIENCE DIRECT®
Journal of the Mechanics and Physics of solids
53 (2005) 495–523
JOURNAL OF THE MECHANICS AND PHYSICS OF SOLIDS
www.elsevier.com/locate/jmps

Finite element simulations of martensitic phase transitions and microstructures based on a strain softening model

A.V. Idesman[a,*], V.I. Levitas[a], D.L. Preston[b], J.-Y. Cho[a]

[a]*Department of Mechanical Engineering, Center for Mechanochemistry and Synthesis of New Materials, Texas Tech University, P.O. Box 41021, Lubbock, TX 79409-1021, USA*
[b]*Applied Physics Division, Los Alamos National Laboratory, Los Alamos, NM 87545, USA*

Received 26 January 2004; received in revised form 4 October 2004; accepted 5 October 2004

Abstract

A new approach for modeling multivariant martensitic phase transitions (PT) and martensitic microstructure (MM) in elastic materials is proposed. It is based on a thermomechanical model for PT that includes strain softening and the corresponding strain localization during PT. Mesh sensitivity in numerical simulations is avoided by using rate-dependent constitutive equations in the model. Due to strain softening, a microstructure comprised of pure martensitic and austenitic domains separated by narrow transition zones is obtained as the solution of the corresponding boundary value problem. In contrast to Landau–Ginzburg models, which are limited in practice to nanoscale specimens, this new phase field model is valid for scales greater than 100 nm and without upper bound. A finite element algorithm for the solution of elastic problems with multivariant martensitic PT is developed and implemented into the software ABAQUS. Simulated microstructures in elastic single crystals and polycrystals under uniaxial loading are in qualitative agreement with those observed experimentally.

Keywords: Martensitic phase transitions; Finite elements; Strain softening; Microstructure

*Corresponding author. Tel.: +1 806 7420970; fax: +1 413 6181802.
E-mail address: alexander.idesman@coe.ttu.edu (A.V. Idesman).

0022-5096/$ - see front matter © 2004 Elsevier Ltd. All rights reserved.
doi:10.1016/j.jmps.2004.10.001

1. Introduction

The martensitic microstructure (MM) that is formed, e.g., in a steel or a shape memory alloy (SMA) as a result of a martensitic PT determines the physical and deformation properties of the material, and possible engineering applications. One of the goals of computational material design is the formation of a desired MM (Olson, 1997). The MM is determined by crystallography, and the external and internal stresses and their relaxation mechanisms. Research on the modeling of martensitic phase transition (PT) in elastic materials (such as SMA) can be subdivided into the following three categories:

(a) Ginzburg–Landau or phase field theory; see Artemev et al. (2000, 2001), Saxena et al. (1997), Rasmussen et al. (2001), Wang and Khachaturyan (1997), Chen and Shen (1998), and others. Phase field theory can describe the formation of a complicated microstructure consisting of austenite and m martensitic variants. The main advantage of this approach is that it is unnecessary to develop special computational algorithms for tracking multiple sharp interfaces between austenite and martensitic variants, as well as between martensitic variants themselves. Diffuse interfaces appear as solutions of the evolution equations for the order parameters and their width is determined by the gradient energy term. The main problem is that for PT in steel and SMA the widths of the interfaces between the martensitic variants and between austenite and martensitic variants are ~ 1 nm. Resolution of the order parameter variation requires at least three computational cells across the interface (Chen and Shen, 1998), thus only single- or poly-nanocrystals can be treated, while the grain sizes in typical engineering materials are 10–1000 μm.

(b) Thermomechanical phenomenological models; see Thamburaja and Anand (2001), Boyd and Lagoudas (1996a, b), Buisson et al. (1991), Siredey et al. (1999), Govindjee and Miehe (2001), Hall and Govindjee (2002), Levitas and Stein (1997), Levitas et al. (1999), Lim and McDowell (2002), and others. This class of models is based on the introduction of the volume fraction of martensitic variants and the treatment of materials with PT as composites with varying volume fractions. Martensitic PT are modeled in terms of a continuous distribution of volume fraction of martensitic variants rather than a discrete MM.

(c) Elastoplastic models with strain softening applied to the simulation of martensitic PT; see Beissel and Belytschko (1996), and Shaw (2000). Strain softening leads to the formation of domains with localized strains that resemble microstructures observed during PTs. Beissel and Belytschko (1996) solve several 1D and 2D model problems on microstructure formation in a viscoplastic material with an unstable (strain softening) stress–strain curve. In Shaw (2000), macroscopic "nucleation" and interface propagation in polycrystalline NiTi was studied. However, the standard rate-dependent (Beissel and Belytschko, 1996) and rate-independent (Shaw, 2000) elastoplastic models with strain softening are just ersatz models that do not account for thermomechanics or the crystallography of multivariant martensitic PT, and therefore cannot describe certain essential features of martensitic PT. We mention also an approach for the description of dislocation

patterns based on the minimization of a multi-well pseudoelastic energy suggested by Ortiz and Repetto (1999).

In this paper, we develop a phase field model and a numerical algorithm for the evolution of multivariant MM in single crystals and polycrystals at scales greater than 100 nm and without upper bound. The volume fraction of the austenite is the order parameter (i.e. parameter responsible for instability), while the volume fractions of martensitic variants are just internal variables. Our model resembles known thermomechanical phenomenological models. However, one distinctive feature of our model is that qualitatively different results are obtained due to inclusion of strain softening due to PT from austenite to martensite, as in the case of the Landau–Ginzburg approach (see the representative stress–strain curve in Fig. 1). As a consequence of this instability, the calculated value of the volume fraction of austenite takes values 0 or 1 over most of the specimen and values between 0 and 1 in small transition regions. In contrast to known thermomechanical phenomenological models, which give only an averaged phase distribution, our model predicts the discrete MM, as in the Landau–Ginzburg approach. In contrast to the Landau–Ginzburg approach, which includes a gradient term corresponding to the surface energy (the scale dependent parameter), our model includes the surface energy in an averaged sense through the coefficients in the thermodynamic potential and does not explicitly contain scale dependent material parameters.

Finite element simulations based on the developed model exhibit the formation of MM qualitatively similar to that observed experimentally. An interesting feature of the simulated microstructure evolution is that, under monotonic uniaxial loading, some martensitic plates that appear during the initial stages of the PT later disappear, i.e., direct and reverse PTs occur simultaneously. This behavior cannot be obtained in models that neglect the discrete MM. Our preliminary results with a similar model are also published in (Levitas et al., 2004).

This paper has the following structure. Our thermomechanical model for multivariant martensitic PT is derived and discussed in Section 2. The model incorporates strain softening and corresponding instability during a PT. Physically motivated kinetic equations for the rate of transformation from each phase to any

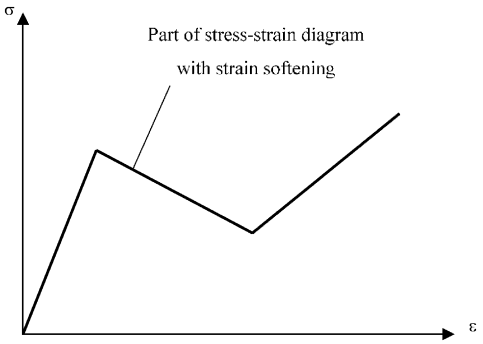

Fig. 1. Stress–strain curve including a strain softening part.

other one ensure also a regularization of the unstable material response, similar to viscoplastic regularization (Beissel and Belytschko, 1996; Needleman, 1988). The complete formulation of the PT problem resembles the system of equations for multisurface viscoplasticity. In Section 3 a finite element algorithm for the modeling of PT in elastic materials based on our thermomechanical model is described. It includes the numerical scheme for the integration of the constitutive equations for multivariant PT and the general Newton–Raphson iteration scheme for the solution of the global system of nonlinear equations. The algorithm is implemented into the finite element (FE) code ABAQUS (2001). Numerical simulations of multivariant martensitic PT in single crystal and polycrystal plates are described in Section 4. The morphology and evolution of the microstructure during martensitic PT are modeled and analyzed.

Coordinate-free tensor notation is used throughout this paper. Vectors and tensors are denoted in boldface type, $\boldsymbol{A}\cdot\boldsymbol{B}$ and $\boldsymbol{A}{:}\boldsymbol{B}$ are the contraction of tensors over one and two indices, $dev\,\boldsymbol{A}$ is the deviatoric part of $\boldsymbol{A}$, and $\dot{\boldsymbol{A}}$ is the material time derivative of $\boldsymbol{A}$.

2. Thermomechanical models of PT

In this section we derive and discuss our phenomenological model for multivariant martensitic PT in elastic materials. A typical martensitic unit consists of alternating planar slabs of two martensitic variants, often twin-related. Since the slab thickness is $d \simeq 10\,\text{nm}$, it is impractical to model each of the thousands of layers in a mm-sized sample. We consider a representative volume of size $l \simeq 10d \simeq 100\,\text{nm}$ comprised of austenite and, in general, m martensitic variants. The Helmholtz free energy ψ of the mixture of austenite and m martensitic variants is assumed to be of the form

$$\psi(\boldsymbol{\varepsilon}_e, c_i, \theta) = \psi_{el}(\boldsymbol{\varepsilon}_e, c_i) + \sum_{i=0}^{m} c_i \psi_i^{\theta}(\theta) + \psi_{in}(c_i). \tag{1}$$

Here c_0 is the volume fraction of austenite (the subscript 0 always denotes austenite), c_i is the volume fraction of the ith Bain strain martensitic variant, $i = 1, 2, \ldots, m$, $c = \sum_{i=1}^{m} c_i$ is the volume fraction of martensite, $\psi_{el}(\boldsymbol{\varepsilon}_e, c_i)$ is the elastic part of the Helmholtz free energy of the mixture, $\psi_i^{\theta}(\theta)$, where θ is the temperature, is the thermal part of the Helmholtz free energy of the ith phase ($\psi_i^{\theta} = \psi_j^{\theta} = \psi_M^{\theta}$ for $i,j > 0$), $\psi_{in}(c_i)$ is the contribution to the free energy of the mixture due to the interactions between austenite and all martensitic variants (energy of internal stresses and the phase interface energy), and $\boldsymbol{\varepsilon}_e$ is the elastic strain of the mixture.

We assume

$$\psi_{in}(c_i) = \sum_{i=0}^{m} \sum_{j=0}^{m} A_{ij} c_i c_j \geqslant 0, \tag{2}$$

where $A_{ij} = A_{ji}$ are material parameters. We can write $A_{ij} = A_{ij}^{e} + A_{ij}^{i}$, where A_{ij}^{e} is due to elastic interactions between phases and A_{ij}^{i} is due to interface energy; see Huo

and Mueller (1993). The parameters A_{ij}^{e} depend on the elastic properties of the austenite and the martensitic variants, and on elastic incompatibility across the interfaces. They can be estimated from known micromechanical models (see, e.g., Kohn, 1991; Siredey et al., 1999; Govindjee et al., 2002; Hall and Govindjee, 2002; Levitas et al., 1998, 1999). Let us analyze the coefficients A_{ij} in (2). If only one homogeneous phase is present, then $\psi_{\text{in}}(c_i)=0$, which results in $A_{ii}=0$. If $c_k\neq 0$ and $c_l\neq 0$ and all other $c_i=0$, then the condition $\psi_{\text{in}}(c_i)\geqslant 0$ results in $A_{kl}\geqslant 0 \forall k\neq l$. As all martensitic variants are connected by the symmetry operations of the austenite, their interactions with the austenite are all the same, hence $A_{0i}=A/2$ for $i\neq 0$. Consequently, the interaction free energy is

$$\psi_{\text{in}}(c_i)=Acc_0+\sum_{i=1}^{m}\sum_{j=1}^{m}A_{ij}c_ic_j\geqslant 0,\quad A>0,\quad A_{ij}\geqslant 0,\quad A_{ii}=0. \tag{3}$$

The condition that $\psi_{\text{in}}>0$ for $c_0\neq 0$ and $c_l\neq 0$ (all other $c_i=0$) leads to the inequality $A>0$.

We use the additive decomposition of the total strain, $\boldsymbol{\varepsilon}$, into elastic, $\boldsymbol{\varepsilon}_{\text{e}}$, and transformation, $\boldsymbol{\varepsilon}_{\text{t}}$, parts; see Eq. (26). The transformation strain $\boldsymbol{\varepsilon}_{\text{t}}$ is given by Eq. (27) where $\boldsymbol{\varepsilon}_{\text{t}i}$ is the Bain transformation strain that transforms the crystal lattice of the austenite into the crystal lattice of martensitic variant i. The list of Bain strains for PTs between various crystal lattices can be found in Bhattacharyya and Kohn (1996) and Pitteri and Zanzotto (2003). For the derivation of a PT criterion for direct and reverse transformations between austenite and any martensitic variant and between any pair of martensitic variants we use the second law of thermodynamics in the form of the Plank inequality

$$D=\boldsymbol{\sigma}:\dot{\boldsymbol{\varepsilon}}-\dot{\psi}-s\dot{\theta}\geqslant 0, \tag{4}$$

where D is the dissipation rate, $\boldsymbol{\sigma}$ is the stress tensor, and s is the entropy. Inserting Eqs. (1), (3), (26), and $c_0=1-\sum_{i=1}^{m}c_i$ into Eq. (4), and assuming that D is independent of $\dot{\boldsymbol{\varepsilon}}_{\text{e}}$ and $\dot{\theta}$, we obtain $\boldsymbol{\sigma}=\partial\psi/\partial\boldsymbol{\varepsilon}_{\text{e}}$, $s=-\partial\psi/\partial\theta$, and the dissipation rate D reduces to

$$D=\sum_{i=1}^{m}X_i\dot{c}_i, \tag{5}$$

where

$$X_i=\boldsymbol{\sigma}:\boldsymbol{\varepsilon}_{\text{t}i}-\frac{\partial\psi_{\text{el}}}{\partial c_i}-(\psi_i^{\theta}-\psi_0^{\theta})-A(1-2c)-2\sum_{k=1}^{m}A_{ik}c_k \tag{6}$$

is the driving force for changes in $\dot{c}_i$. Defining $\dot{c}_{ij}$ as the rate of change of the volume fraction c_i due to a transition from phase j to i, we have the relations

$$\dot{c}_i=\sum_{j=0}^{m}\dot{c}_{ij},\quad \dot{c}_{ij}=-\dot{c}_{ji},\quad \dot{c}_{ii}=0. \tag{7}$$

Then

$$D = \sum_{i=1}^{m} X_{i0}\dot{c}_{i0} + \sum_{j=1}^{m-1}\sum_{i=j+1}^{m} X_{ij}\dot{c}_{ij}, \tag{8}$$

where $X_{i0} = X_i$ is the driving force for the austenite to variant i PT (if $X_{i0} > 0$) or for the variant i to austenite PT (if $X_{i0} < 0$), and

$$X_{ij} = X_i - X_j = \boldsymbol{\sigma} : (\boldsymbol{\varepsilon}_{ti} - \boldsymbol{\varepsilon}_{tj}) - \left(\frac{\partial \psi_{el}}{\partial c_i} - \frac{\partial \psi_{el}}{\partial c_j}\right) - 2\sum_{k=1}^{m}(A_{ik} - A_{jk})c_k \tag{9}$$

is the driving force for the variant $j \to$ variant i transformation (if $X_{ij} > 0$) or the variant $i \to$ variant j transformation (if $X_{ij} < 0$). We consider three models for the PT criterion and the kinetic equations for the $\dot{c}_{ij}$.

2.1. Model A: no threshold for the driving forces

In this model the PT criterion and the kinetic equations for the $\dot{c}_{ij}$ are written as follows:

$$\begin{aligned} &X_{ij} \geqslant 0 \quad \text{and} \quad \left\{\begin{array}{l} 0 \leqslant c_i < 1 \\ 0 < c_j \leqslant 1 \end{array}\right\} \\ &\qquad\qquad\qquad\qquad \Rightarrow \quad \dot{c}_{ij} = \lambda_{ij} X_{ij}, \\ &X_{ij} \leqslant 0 \quad \text{and} \quad \left\{\begin{array}{l} 0 < c_i \leqslant 1 \\ 0 \leqslant c_j < 1 \end{array}\right\} \\ &X_{ij} \geqslant 0 \quad \text{and} \quad \{c_i = 1 \quad or \quad c_j = 0\} \\ &X_{ij} \leqslant 0 \quad \text{and} \quad \{c_i = 0 \quad or \quad c_j = 1\} \quad \Rightarrow \quad \dot{c}_{ij} = 0, \end{aligned} \tag{10}$$

where λ_{ij} are kinetic coefficients. Rate-dependent (rather than rate-independent) kinetics follows from the thermally activated mechanism of martensite growth and the rate-dependent kinetics equation for interface motion; see Olson and Cohen (1986). These coefficients λ_{ij} can be determined by comparing calculations and experiments for some non-stationary process like the interface propagation under prescribed stresses and temperature. We chose such λ_{ij} that the characteristic rate of phase transformations in the narrow transformation zone significantly exceeds the characteristic rate of external loading. We found that for chosen λ_{ij} numerical results (the martensite distribution and the macroscopic stress–strain curve) are approximately the same for the macroscopic deformation rate in the range (0.1–0.5) $\times 10^8\,\mathrm{s}^{-1}$.

Assuming fulfillment of the Onsager reciprocity relations, we obtain $\lambda_{ij} = \lambda_{ji}$. These relationships describe direct and reverse transformations between variants i and j $(i,j = 0,1,2,\ldots,m)$. Since all martensitic variants are connected by the

symmetry operations of the austenite, their kinetic coefficients for transformations to austenite are all the same, i.e., $\lambda_{0i} = \lambda_{0j} = \lambda$.

We now determine the necessary conditions for which the model describes a microstructure consisting only of regions of austenite ($c = 0$) and martensitic variants ($c = 1$) without mixed regions of austenite and martensite ($0 < c < 1$) for phase equilibrium, that is, when $\dot{c}_{i0} = 0$. The analysis is simpler if we introduce the Gibbs potential $G := \psi - \boldsymbol{\sigma} : \boldsymbol{\varepsilon}$. Then it is easy to check that

$$X_i = X_{i0} = -\frac{\partial G}{\partial c_i}, \quad \dot{c}_{i0} = \lambda X_{i0} = -\lambda \frac{\partial G}{\partial c_i}. \tag{11}$$

Because we admit an equilibrium mixture of martensitic variants, but do not admit an equilibrium mixture of austenite and martensite, it is convenient to introduce new variables that characterize variant–variant transformations at fixed c. Consider the m-dimensional space of volume fractions of martensitic variants and the vector $\boldsymbol{c} = \{c_i\}$. The vector $\mathbf{1} = \{1\}$ and the corresponding unit vector $\boldsymbol{n} = \{1\}/\sqrt{m}$ are equally inclined to all coordinate axes. The projection of $\boldsymbol{c}$ on $\boldsymbol{n}$ is $\boldsymbol{c} \cdot \boldsymbol{n} = \sum_{i=1}^{m} c_i/\sqrt{m} = c/\sqrt{m}$. We decompose $\boldsymbol{c}$ into $(c/\sqrt{m})\boldsymbol{n}$ and $\bar{\boldsymbol{c}} := \boldsymbol{c} - (c/\sqrt{m})\boldsymbol{n}$ ($\bar{c}_i = c_i - c/m$), which is in the plane orthogonal to $\boldsymbol{n}$, i.e., $\bar{\boldsymbol{c}} \cdot \mathbf{1} = \sum_{i=1}^{m} \bar{c}_i = 0$. Consequently, a change in $\bar{c}_i$ does not affect the volume fraction of martensite c. Thus, the volume fraction of martensite c varies along the $\mathbf{1}$ axis, which we will refer to as the austenite–martensite axis. The plane orthogonal to axis $\mathbf{1}$ will be called the variant–variant plane because changes in the $\bar{c}_i$ in this plane represent variant–variant transformations at constant total martensite fraction c. The austenite–martensite axis and the variant–variant plane are analogous to the hydrostatic axis and deviatoric stress plane in stress space. Substituting $c_i = \bar{c}_i + c/m$ in the expression for G and taking into account $\partial \bar{c}_j/\partial c_i = \delta_{ji} - 1/m$, Eq. (11), we obtain

$$\dot{c}_{i0} = -\lambda \frac{\partial G}{\partial c_i} = -\lambda \frac{\partial G}{\partial c} - \lambda \frac{\partial G}{\partial \bar{c}_i} + \frac{\lambda}{m} \sum_{k=1}^{m} \frac{\partial G}{\partial \bar{c}_k}. \tag{12}$$

Summation over i in Eq. (12) results in

$$\dot{c} = \sum_{i=1}^{m} \dot{c}_{i0} = -\lambda m \frac{\partial G}{\partial c}. \tag{13}$$

It follows from Eq. (13) that austenite–martensite phase equilibrium corresponds to a stationary point of the Gibbs potential G in c. Such an equilibrium is stable if G has a minimum in c.

We now find the conditions for which the Gibbs potential G does not have a minimum for $0 < c < 1$, i.e., only $c = 0$ or 1 or both are possible minima of the Gibbs potential G. In contrast to the nanoscale Landau theory (Levitas and Preston, 2002a, b; Levitas et al., 2003), we do not impose the constraint that each martensitic variant minimizes the Gibbs potential. Substituting $c_i = \bar{c}_i + c/m$ in Eq. (3) for ψ_{in},

we obtain

$$\psi_{\text{in}} = A(1-c)c + \frac{c^2}{m^2}\sum_{i=1}^{m}\sum_{j=1}^{m} A_{ij} + 2\,\frac{c}{m}\sum_{i=1}^{m}\sum_{j=1}^{m} A_{ij}\bar{c}_i + \sum_{i=1}^{m}\sum_{j=1}^{m} A_{ij}\bar{c}_i\bar{c}_j \geqslant 0. \tag{14}$$

It follows from (14) and Eqs. (1), (3), (26), and (27) that the Gibbs potential has the following form:

$$\begin{aligned} G = \psi - \boldsymbol{\sigma} : \boldsymbol{\varepsilon} = G_{\text{el}}(\boldsymbol{\sigma}, c, \bar{c}_i, \theta) - \frac{c}{m}\,\boldsymbol{\sigma} : \sum_{i=1}^{m} \boldsymbol{\varepsilon}_{\text{t}i} - \boldsymbol{\sigma} : \sum_{i=1}^{m} \boldsymbol{\varepsilon}_{\text{t}i}\bar{c}_i \\ + (1-c)\psi_0^{\theta}(\theta) + c\psi_M^{\theta}(\theta) + A(1-c)c \\ + \frac{c^2}{m^2}\sum_{i=1}^{m}\sum_{j=1}^{m} A_{ij} + 2\,\frac{c}{m}\sum_{i=1}^{m}\sum_{j=1}^{m} A_{ij}\bar{c}_i + \sum_{i=1}^{m}\sum_{j=1}^{m} A_{ij}\bar{c}_i\bar{c}_j, \end{aligned} \tag{15}$$

where $G_{\text{el}} \coloneqq \psi_{\text{el}} - \boldsymbol{\sigma} : \boldsymbol{\varepsilon}_{\text{e}}$ is the complementary elastic energy. We assume that the expression for G_{el} can be expressed in the form $G_{\text{el}} = P_0 + P_1 c + P_2 c^2$, where the P_i are stress, temperature, and $\bar{c}_i$ dependent parameters determined from the expression for the effective elastic compliances. Then

$$\begin{aligned} &G = B_0 + B_1 c + B_2 c^2, \quad B_0 = P_0 - \boldsymbol{\sigma} : \sum_{i=1}^{m} \boldsymbol{\varepsilon}_{\text{t}i}\bar{c}_i + \psi_0^{\theta}(\theta) + \sum_{i=1}^{m}\sum_{j=1}^{m} A_{ij}\bar{c}_i\bar{c}_j, \\ &B_1 = P_1 - \frac{1}{m}\,\boldsymbol{\sigma} : \sum_{i=1}^{m} \boldsymbol{\varepsilon}_{\text{t}i}\bar{c}_i - \psi_0^{\theta}(\theta) + \psi_M^{\theta}(\theta) + A + \frac{2}{m}\sum_{i=1}^{m}\sum_{j=1}^{m} A_{ij}\bar{c}_i, \\ &B_2 = P_2 - A + \frac{1}{m^2}\sum_{i=1}^{m}\sum_{j=1}^{m} A_{ij}. \end{aligned} \tag{16}$$

The Gibbs potential will have no minima in the interval $0 \leqslant c \leqslant 1$ other than those at $c = 0$ or $c = 1$ if $B_2 < 0$. Plots of $G(c)$ for different B_i are shown in Fig. 2. Consequently, the constraint $B_2 < 0$, which expresses instability of phase equilibrium for $0 < c < 1$, is equivalent to

$$A > P_2 + \frac{1}{m^2}\sum_{i=1}^{m}\sum_{j=1}^{m} A_{ij} \tag{17}$$

in our model.

2.2. Model B: non-zero threshold for the driving forces

In most microscale theories of PT, a dissipative threshold is introduced for the driving forces (Buisson et al., 1991; Boyd and Lagoudas, 1996a, b; Lim and McDowell, 2002; Levitas et al., 1998, 1999; Thamburaja and Anand, 2001; Govindjee and Miehe, 2001, and others). The physical mechanisms responsible for such a threshold include: the athermal component of the interaction of a moving

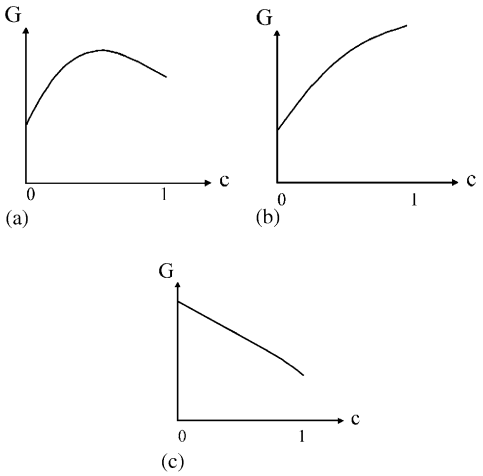

Fig. 2. Plot of the Gibbs energy versus c for different parameters B_i: (a) stable austenite and metastable martensite; (b) stable martensite and unstable austenite; (c) stable austenite and unstable martensite.

interface with various defects, e.g., point defects (solute and impurity atoms, vacancies), dislocations, grain, subgrain, and twin boundaries, and precipitates; emission of acoustic waves; and the Peierls barrier. In a model with a dissipative threshold the PT criterion and the kinetic equations for the $\dot{c}_{ij}$ can be written as follows (similar to viscoplastic models in plasticity):

$$|X_{ij}|>k_{ij} \quad \Rightarrow \quad \dot{c}_{ij}=\lambda_{ij}\,\mathrm{sign}(X_{ij})(|X_{ij}|-k_{ij}), \tag{18}$$

$$|X_{ij}|\leqslant k_{ij} \quad \Rightarrow \quad \dot{c}_{ij}=0, \tag{19}$$

where k_{ij} (we assume $k_{ij}=k_{ji}$) is the given critical value of the driving force for the transition from phase j to the phase i. Surface energy can be effectively included in k_{ij} as an alternative or addition to A_{ij}. The model reduces to the previous one for $k_{ij}=0$. Below we will show that the model with non-zero k_{ij} can also lead to the formation of microstructure due to strain softening (as in viscoplastic models with softening, see Beissel and Belytschko, 1996).

We assume below that the elastic properties of the austenite and the martensite are identical and isotropic, hence

$$\psi_{\mathrm{el}}=\tfrac{1}{2}\boldsymbol{\varepsilon}_{\mathrm{e}}:\boldsymbol{C}:\boldsymbol{\varepsilon}_{\mathrm{e}}, \tag{20}$$

where $\boldsymbol{C}$ is the fourth-order isotropic elastic tensor. Let martensitic variants i and j be kinematically compatible, i.e., the interface between them is an invariant plane. This is true, in particular, for twin-related variants. Such variants do not generate internal stresses, thus the corresponding A^{e}_{ij} is equal to zero. The variant–variant interface energy in this case is also small, so we assume $A^{\mathrm{i}}_{ij}=0$ as well; hence $A_{ij}=A^{\mathrm{e}}_{ij}+A^{\mathrm{i}}_{ij}=0$ and $X_{ij}=\boldsymbol{\sigma}:(\boldsymbol{\varepsilon}_{\mathrm{t}i}-\boldsymbol{\varepsilon}_{\mathrm{t}j})$. We cannot assume $A=A^{\mathrm{e}}+A^{\mathrm{i}}=0$ because martensite is usually incompatible with austenite, thus the austenite–martensite

interface energy is larger than the variant–variant interface energy (i.e. $A^{\mathrm{i}}>0$). Even if austenite and a habit plane martensitic variant, consisting of two twin-related variants, are compatible, we cannot assume $A^{\mathrm{e}}=0$, because A^{e} characterizes the incompatibility between austenite and a single Bain-strain martensitic variant. A compatible interface between austenite and a habit plane variant may appear as a solution of the boundary-value problem. Thus the instability condition (17), which reduces to $A>0$, is valid.

The formulation of boundary value problems for elastic materials with PT reduces to the system given in Box 1 where $\boldsymbol{u}$ is the displacement vector, $(\partial \boldsymbol{u}/\partial \boldsymbol{x})_{\mathrm{s}}$ is the symmetric part of the tensor $\partial \boldsymbol{u}/\partial \boldsymbol{x}$, $\bar{\boldsymbol{t}}$ is the traction on the boundary G_σ, $\boldsymbol{n}$ is the unit normal to the boundary G_σ, $\bar{\boldsymbol{u}}$ is the given displacement on the boundary G_u, t is time, and c_i^* is the initial volume fraction of phase i.

Because of the conditions $\dot{c}_{ij}=-\dot{c}_{ji}$, the total volume fraction $\sum_{i=0}^{m} c_i$ does not change in time, which together with $\sum_{i=0}^{m} c_i^*=1$ implies $\sum_{i=0}^{m} c_i=1$. Therefore, if $c_i\geqslant 0$ for $i=0,1,2,\ldots,m$ then the inequality $c_i\leqslant 1$ is automatically satisfied.

In order to show that this model can describe strain softening during a PT we consider for simplicity a material with a single martensitic variant ($m=1$) under one-dimensional tension with $\sigma_{11}=\bar{\sigma}$ and $\sigma_{12}=\sigma_{13}=\sigma_{22}=\sigma_{23}=\sigma_{33}=0$. The initiation of the PT and its continuation at an infinitesimal rate correspond to the condition $X_{10}-k_{10}=0$, which, according to Eq. (6), reduces to

$$\bar{\sigma}\bar{\varepsilon}_{\mathrm{t}}-(\psi_1^{\theta}-\psi_0^{\theta})-A(1-2c)-k_{10}=0, \tag{21}$$

where $\bar{\varepsilon}_{\mathrm{t}}=(\boldsymbol{\varepsilon}_{\mathrm{t}})_{11}$ is the normal component of the transformation strain along the tensile axis. According to Hooke's law, Eq. (29), and Eqs. (26) and (27) (see Box 1) it follows that

$$\bar{\sigma}=E(\bar{\varepsilon}-c\bar{\varepsilon}_{\mathrm{t}}), \tag{22}$$

where $\bar{\varepsilon}=\varepsilon_{11}$ is the normal component of the total strain $\boldsymbol{\varepsilon}$ along the tensile axis and E is the Young's modulus. Eliminating c from Eq. (21) by means of Eq. (22) we get

$$\bar{\sigma}(\bar{\varepsilon}_{\mathrm{t}}^2-2A/E)+2A\bar{\varepsilon}-[(\psi_1^{\theta}-\psi_0^{\theta})+A+k_{10}]\bar{\varepsilon}_{\mathrm{t}}=0. \tag{23}$$

Eq. (23) describes the relationship between the stress $\bar{\sigma}$ and total strain $\bar{\varepsilon}$ during the PT. Let us analyze this equation. If the material parameter A satisfies the inequality

$$A<E\bar{\varepsilon}_{\mathrm{t}}^2/2 \tag{24}$$

then Eq. (23) describes strain softening during the PT (see Fig. 1), that is

$$\frac{\partial\bar{\sigma}}{\partial\bar{\varepsilon}}=\frac{-2A}{\bar{\varepsilon}_{\mathrm{t}}^2-2A/E}<0 \tag{25}$$

and the stress $\bar{\sigma}$ decreases with increasing strain $\bar{\varepsilon}$ (the constant A in Eq. (3) is always positive because ψ_{in} is positive). In this paper inequality (24) is assumed to hold for the maximum normal component of the transformation strain $\boldsymbol{\varepsilon}_{\mathrm{t}i}$ ($i=1,2,\ldots,m$) in the three-dimensional case, thus the tangent moduli $\partial\boldsymbol{\sigma}/\partial\boldsymbol{\varepsilon}$ are not positive definite, which corresponds to material instability. This instability leads to strain localization and the formation of a MM.

The upper bound for the parameter A in Eq. (24) is the maximum possible elastic energy density, $\sim E\varepsilon_y^2/2$, where ε_y is the elastic strain at plastic yielding. For the SMAs NiTi and CuZnAl, $\varepsilon_y \sim 0.01$, and $\varepsilon_y \sim 0.001$ for steel, while $\bar{\varepsilon}_t \sim 0.1$ for both SMAs and steel, therefore $A \ll E\bar{\varepsilon}_t^2/2$.

Note that inequality (24) is not related to the material instability condition (17), which reduces to $A > 0$. If inequality (24) is not fulfilled, the stress–strain curve is as shown in Fig. 3b. Despite the positive tangent moduli, this model also exhibits an instability. The reason for the instability is that the driving force for the PT, X_{10}, grows with increasing volume fraction. Consequently, after satisfying the PT criterion, an accelerated PT will occur at constant stress or the stress must decrease to sustain an equilibrium PT (a PT with infinitesimal rates $\dot{c}_i$), which is a PT satisfying $X_{10} = k_{10}$. During an equilibrium PT, not only the stress but also the total strain decreases because the reduction in elastic strain exceeds the transformation strain.

We note that model A with $k = 0$ also leads to a stress–strain curve with strain softening (Fig. 3c). This follows from (23) for $k_{10} = 0$.

In a finite sample the local stresses vary significantly during the transformation process and both direct and reverse PT can occur at different points even under one-dimensional monotonic loading (see Section 4). Because of the stress hysteresis due to k_{10}, it is possible that the PT will be arrested at some intermediate c, i.e., $0 < c < 1$.

We did not study the general case $A_{ij} \neq 0$, but for $A_{ij} = 0$ and $X_{ij} = \boldsymbol{\sigma} : (\boldsymbol{\varepsilon}_{ti} - \boldsymbol{\varepsilon}_{tj})$, our thermodynamic potential does not have instabilities associated with transitions

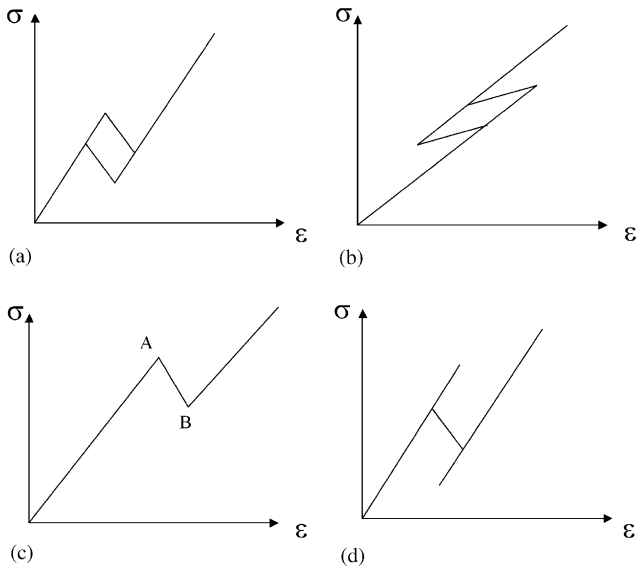

Fig. 3. Schematic stress–strain curves for direct and reverse PT for a single variant under one-dimensional tension and slow deformation for different values of the threshold k_{10}: (a) $k_{10} \neq 0$ and inequality (24) is satisfied; (b) $k_{10} \neq 0$ and inequality (24) is not satisfied; (c) $k_{10} = 0$; (d) k_{10} discontinuous.

between martensitic variants. The martensite at each point can consist of several martensitic variants with volume fractions determined from the solution of the corresponding boundary-value problem. Thus, the volume fraction of martensite c is the only order parameter (i.e. parameter responsible for instability); the $\bar{c}_i$ are just internal variables.

2.3. Model C: discontinuous threshold for the driving forces

To avoid regions at some intermediate c we may employ a discontinuous threshold k_{0i}. Specifically, $k_{0i} = k_{i0}$ is non-zero if $c_0 = 0$ or $c_i = 0$, and $k_{0i} = k_{i0} = 0$ if $c_i c_0 \neq 0$, i.e., after satisfying the $0 \leftrightarrow i$ PT criteria at $c_0 = 0$ or $c_i = 0$, there is no barrier for the $0 \leftrightarrow i$ PT (Fig. 3d). At the same time the threshold k_{ij} can be non-zero for $i \neq 0$ and $j \neq 0$. Models A and C are similar in that the PT at any point will not be arrested at some intermediate value of c.

Note that in PT models without instabilities (Buisson et al., 1991; Boyd and Lagoudas, 1996a, b; Lim and McDowell, 2002; Levitas et al., 1998, 1999; Thamburaja and Anand, 2001; Govindjee and Miehe, 2001), the introduction of the threshold k_{i0} is the only way to describe stress hysteresis and dissipation due to austenite–martensite PT. For our models A and C with instability, stress hysteresis is absent as well for local direct and reverse equilibrium PT. However, because of the instability of homogeneous deformations and PT, there is macroscopic stress hysteresis in a finite specimen for $k_{i0} = 0$. Indeed, an austenite–martensite interface cannot propagate through a specimen for the direct PT at a stress lower than σ_A, and it cannot move back for the reverse PT at stresses higher than σ_B; see Fig. 3c and Truskinovsky (1994). Hence, macroscopic stress hysteresis and the corresponding dissipation can occur at zero threshold if the PT model incorporates an instability.

Box 1. Problem formulation

1. Kinematics

Decomposition of the total strain $\boldsymbol{\varepsilon}$:

$$\boldsymbol{\varepsilon} := \left(\frac{\partial \boldsymbol{u}}{\partial \boldsymbol{x}}\right)_s = \boldsymbol{\varepsilon}_e + \boldsymbol{\varepsilon}_t. \tag{26}$$

Transformation strain $\boldsymbol{\varepsilon}_t$:

$$\boldsymbol{\varepsilon}_t = \sum_{i=1}^{m} \boldsymbol{\varepsilon}_{ti} c_i. \tag{27}$$

Volume fractions and their rates:

$$c = \sum_{i=1}^{m} c_i, \quad \sum_{i=0}^{m} c_i = c_0 + c = 1, \quad \dot{c}_i = \sum_{j=0}^{m} \dot{c}_{ij}, \dot{c}_{ij} = -\dot{c}_{ji}, \quad c_i \geqslant 0. \tag{28}$$

2. Constitutive equation

$$\text{Elastic Hooke's law} \quad \boldsymbol{\sigma} = \boldsymbol{C} : \boldsymbol{\varepsilon}_e = K I_1(\boldsymbol{\varepsilon}_e)\boldsymbol{I} + 2G \operatorname{dev} \boldsymbol{\varepsilon}_e. \tag{29}$$

Phase transition criterion:
For a transition from austenite 0 to martensitic variant i (or the reverse transition).

$$f_{i0}(\boldsymbol{\sigma}, c, \theta) \equiv |X_{i0}| - k_{i0} = |\boldsymbol{\sigma} : \boldsymbol{\varepsilon}_{ti} - (\psi_i^\theta - \psi_0^\theta) - A(1-2c)| - k_{i0} \geqslant 0, \quad i = 1, 2, \ldots, m. \tag{30}$$

For a transition from martensitic variant j to martensitic variant i (or the reverse transition)

$$f_{ij}(\boldsymbol{\sigma}) \equiv |X_{ij}| - k_{ij} = |\boldsymbol{\sigma} : (\boldsymbol{\varepsilon}_{ti} - \boldsymbol{\varepsilon}_{tj})| - k_{ij} \geqslant 0, \quad j = 1, 2, \ldots, m-1, \quad i = j+1, j+2, \ldots, m. \tag{31}$$

Evolution equations for the $\dot{c}_{ij}$:

$$f_{ij}(\boldsymbol{\sigma}, c, \theta) \geqslant 0 \implies \dot{c}_{ij} = \lambda_{ij} \operatorname{sign}(X_{ij})(|X_{ij}| - k_{ij}), \tag{32}$$

$$f_{ij}(\boldsymbol{\sigma}, c, \theta) < 0 \implies \dot{c}_{ij} = 0, \quad j = 0, 1, \ldots, m-1, \quad i = j+1, j+2, \ldots, m. \tag{33}$$

$ModelA: k_{i0} = 0; \quad ModelB: k_{i0} \neq 0; \quad ModelC: k_{i0} = 0 \quad for \quad c_i c_0 \neq 0.$

3. Equilibrium equations (with body forces $\boldsymbol{F}$)

$$\boldsymbol{\nabla} \cdot \boldsymbol{\sigma} + \boldsymbol{F} = 0. \tag{34}$$

4.(a) Boundary conditions

$$\boldsymbol{\sigma} \cdot \boldsymbol{n} = \bar{\boldsymbol{t}}(t) \quad \text{on} \quad G_\sigma, \tag{35}$$

$$\boldsymbol{u} = \bar{\boldsymbol{u}}(t) \quad \text{on} \quad G_u. \tag{36}$$

(b) Initial conditions

$$c_i = c_i^*, \quad \sum_{i=0}^{m} c_i^* = 1. \tag{37}$$

3. Finite element algorithm

We now describe the finite element algorithm for the solution of the system shown in Box 1. Because the solution of this system is similar to the solution of elastoviscoplastic problems we present only the main components of the algorithm: the numerical integration of the constitutive equations for PT and the general Newton–Raphson iterative scheme (see Simo and Hughes (1998) for elastoviscoplastic problems).

The α-method of time integration (Bathe, 1996) is used for the numerical integration of the evolution equations (34)

$$\Delta c_{ij} = \lambda_{ij} \Delta t \operatorname{sign}(X_{ij})(|X_{ij}(\boldsymbol{\sigma}^{n+\alpha}, c^{n+\alpha}, \theta^{n+\alpha})| - k_{ij}), \tag{38}$$

where

$$\boldsymbol{\sigma}^{n+\alpha} = \boldsymbol{\sigma}^{n} + \alpha\Delta\boldsymbol{\sigma} = \boldsymbol{\sigma}^{n} + \alpha\boldsymbol{C} : \Delta\boldsymbol{\varepsilon} - \sum_{r=1}^{m}\sum_{j=0}^{m} \alpha\Delta c_{rj}\boldsymbol{C} : \boldsymbol{\varepsilon}_{tr}, \tag{39}$$

$$c^{n+\alpha} = c^{n} + \alpha\Delta c, \tag{40}$$

$$\theta^{n+\alpha} = \theta^{n} + \alpha\Delta\theta. \tag{41}$$

The constant α varies from 0 to 1: $\alpha = 0$ for the explicit Euler forward method, $\alpha = 0.5$ for the implicit trapezoidal rule, and $\alpha = 1$ for the implicit Euler backward method.

The integration scheme for the constitutive equations (using 'predictor' and 'corrector' like in plasticity) is given in Box 2. Due to the condition $\Delta c_{ij} = -\Delta c_{ji}$, the equality $\sum_{i=0}^{m} c_i = \sum_{i=0}^{m} c_i^* = 1$ is satisfied at all times during the integration procedure. The tangent moduli $\partial\Delta\boldsymbol{\sigma}/\partial\Delta\boldsymbol{\varepsilon}$ consistent with this scheme follow from Eqs. (47)–(49)

$$\frac{\partial\Delta\boldsymbol{\sigma}}{\partial\Delta\boldsymbol{\varepsilon}} = \boldsymbol{C} - \sum_{r=1}^{m}\sum_{j=0}^{m} \frac{\partial\Delta c_{rj}}{\partial\Delta\boldsymbol{\varepsilon}}\boldsymbol{C} : \boldsymbol{\varepsilon}_{tr} = \boldsymbol{C} - \sum_{r=1}^{m}\sum_{j=0}^{m} \boldsymbol{a}_{rj}\boldsymbol{C} : \boldsymbol{\varepsilon}_{tr}, \tag{42}$$

where $\boldsymbol{a}_{rj}$ are the matrices of the coefficients in the representation of Δc_{ij} in terms of $\Delta\boldsymbol{\varepsilon}$. They can be found numerically from the solution of the system of linear algebraic equations (45) and (46). The complete finite element algorithm for the solution of PT problems (similar to the solution of elastoviscoplastic problems, see Simo and Hughes, 1998) based on the Newton–Raphson iterative scheme for the solution non-linear discrete problem is given in Box 3.

The FE software ABAQUS (2001) is used. This software allows a user to encode special constitutive equations (e.g., the PT model in Box 1) in a user material subroutine UMAT.

Box 2. Integration of the constitutive equations

Given: $\boldsymbol{\sigma}^n$, c_i^n, $\Delta\boldsymbol{\varepsilon} = \dot{\boldsymbol{\varepsilon}}\Delta t$ and $\theta^{n+1} = \theta^n + \Delta\theta$

Find: $\boldsymbol{\sigma}^{n+1}$, c_i^{n+1}

1. Compute the trial stress $\boldsymbol{\sigma}^*$

$$\boldsymbol{\sigma}^* = \boldsymbol{\sigma}^n + \boldsymbol{C} : \Delta\boldsymbol{\varepsilon}. \tag{43}$$

2. Check PT criteria (Eqs. (31) and (32))

If $f_{ij}(\boldsymbol{\sigma}^*, c^n, \theta^{n+1}) \leqslant 0$ then $\Delta c_{ij} = 0$ and go to 4.

3. For active phase transformations find Δc_{ij}

$$\text{If} \quad f_{ij}(\boldsymbol{\sigma}^*, c^n, \theta^{n+1}) > 0 \quad \text{and} \quad \left\{ \begin{array}{c} X_{ij}(\boldsymbol{\sigma}^*, c^n, \theta^{n+1}) > 0, \quad c_i < 1 \\ or \\ X_{ij}(\boldsymbol{\sigma}^*, c^n, \theta^{n+1}) < 0, \quad c_i > 0 \end{array} \right\} \quad \text{then :} \tag{44}$$

for a transition from austenite 0 to martensitic variant i (or the reverse transition)

$$\Delta c_{i0} = \lambda_{i0}\Delta t\,\mathrm{sign}(X_{i0})\{|\boldsymbol{\varepsilon}_{ti} : \boldsymbol{\sigma}^n + \alpha\boldsymbol{\varepsilon}_{ti} : \boldsymbol{C} : \Delta\boldsymbol{\varepsilon} - \sum_{r=1}^{m}\sum_{j=0}^{m}\alpha\Delta c_{rj}\boldsymbol{\varepsilon}_{ti} : \boldsymbol{C} : \boldsymbol{\varepsilon}_{tr} - (\psi_i^\theta - \psi_0^\theta) - A + 2A\left(c^n + \alpha\sum_{r=0}^{m}\sum_{p=1}^{m}\Delta c_{rp}\right)| - k_{i0}\Big\}, \quad i = 1,2,\ldots,m; \tag{45}$$

for a transition from martensitic variant j to martensitic variant i (or the reverse transition)

$$\Delta c_{ij} = \lambda_{ij}\Delta t\,\mathrm{sign}(X_{ij})\Big\{|(\boldsymbol{\varepsilon}_{ti} - \boldsymbol{\varepsilon}_{tj}) : \boldsymbol{\sigma}^n + \alpha(\boldsymbol{\varepsilon}_{ti} - \boldsymbol{\varepsilon}_{tj}) : \boldsymbol{C} : \Delta\boldsymbol{\varepsilon} - \sum_{r=1}^{m}\sum_{s=0}^{m}\alpha\Delta c_{rs}(\boldsymbol{\varepsilon}_{ti} - \boldsymbol{\varepsilon}_{tj}) : \boldsymbol{C} : \boldsymbol{\varepsilon}_{tr}| - k_{i0}\Big\},$$
$$j = 1,2,\ldots,m-1, \quad i = j+1, j+2,\ldots,m. \tag{46}$$

or Eqs. (45) and (46) can be expressed as

$$\Delta c_{ij} = \boldsymbol{a}_{ij} : \Delta\boldsymbol{\varepsilon} + b_{if}, \quad j = 0,1,\ldots,m-1, \quad i = j+1, j+2,\ldots,m \tag{47}$$

($\boldsymbol{a}_{ij}$ and b_{ij} are the corresponding matrices and coefficients).

4. Compute c^{n+1}, $\boldsymbol{\sigma}^{n+1}$

$$c_i^{n+1} = c_i^n + \Delta c_i = c_i^n + \sum_{j=0}^{m}\Delta c_{ij}, \tag{48}$$

$$\boldsymbol{\sigma}^{n+1} = \boldsymbol{\sigma}^n + \Delta\boldsymbol{\sigma} = \boldsymbol{\sigma}^n + \boldsymbol{C} : \left(\Delta\boldsymbol{\varepsilon} - \sum_{i=1}^{m}\boldsymbol{\varepsilon}_{ti}\Delta c_i\right) \tag{49}$$

Box 3. Finite element solution algorithm

1. *Initialization at t_n. Data structure*:
Variables at quadrature points $\{\boldsymbol{\sigma}, c_i\}^n$
Initial conditions for displacement vector at nodal points $\{u\}^{n+1} = 0$
Current values of boundary conditions at time t^{n+1}

2. *Let $\{u\}_k^{n+1}$ be the solution at the k-iteration and time step $n+1$.*

2.1. Compute $\{\boldsymbol{\sigma}, c_i\}_k^{n+1}$ at quadrature points (see Box 2)

2.2. Compute the consistent tangents at quadrature points (Eq. (42))

2.3. Compute residuals of the FE equilibrium equation $\{R\}_k^{n+1}$
$\{R\}_k^{n+1} = \{f\}_k^{n+1} - \int_\Omega([B]^t)_k^{n+1}\{\sigma\}_k^{n+1}\,\mathrm{d}\Omega$
($\{f\}_k^{n+1}$ is the standard FE load vector, $[B]_k^{n+1}$ is the standard B-matrix)
IF $||\{R\}_k^{n+1}|| < \mathrm{TOL}$ GO TO 4 (TOL is prescribed)

3. *Solve system*:
$[K]\{\Delta u\}_k^{n+1} = \{R\}_k^{n+1}$,
where $[K] = -\int_\Omega ([B]^t)_k^{n+1}(\partial\Delta\boldsymbol{\sigma}/\partial\Delta\boldsymbol{\varepsilon})[B]_k^{n+1}\,d\Omega$ is the consistent tangent stiffness matrix.
Update: $\{u\}_{k+1}^{n+1} = \{u\}_k^{n+1} + \{\Delta u\}_k^{n+1}$
Set $k = k + 1$ and GO TO 2

4. *Update data structure*:
$\{\boldsymbol{\sigma}, c_i\}^{n+1} = \{\boldsymbol{\sigma}, c_i\}_k^{n+1}$

4. Numerical modeling

All calculations were carried out for 2-D problems using six-node quadratic triangular finite elements with a quadratic approximation for the displacements.

We simulated the formation of MM due to a cubic–tetragonal PT in a plane-strained specimen under uniaxial tension. Two models were used: model B with nonzero thresholds for the driving forces and model C for which the thresholds for the driving forces are discontinuous. Our numerical results for these two models do not differ significantly.

It is assumed that the temperature is homogeneously distributed and does not change during the PT. The cubic–tetragonal PT was constrained to two of its three variants. The transformation strains $\boldsymbol{\varepsilon}_{t1}$ and $\boldsymbol{\varepsilon}_{t2}$ have the following components:

$$(\boldsymbol{\varepsilon}_{t1})_{11} = 0.1, \quad (\boldsymbol{\varepsilon}_{t1})_{22} = -0.1, \quad (\boldsymbol{\varepsilon}_{t1})_{21} = 0, \tag{50}$$

$$(\boldsymbol{\varepsilon}_{t2})_{11} = -0.1, \quad (\boldsymbol{\varepsilon}_{t2})_{22} = 0.1, \quad (\boldsymbol{\varepsilon}_{t2})_{21} = 0; \tag{51}$$

all other components are zero. The following material parameters were used: $E = 2\times10^5$ MPa (Young's modulus), $v = 0.3$ (Poisson ratio), $A = 0.1$ MPa, $\lambda_{10} = \lambda_{20} = \lambda_{21} = 10\,\text{MPa}^{-1}\,\text{s}^{-1}$, $k_{10} = k_{20} = 0.2$ MPa, $k_{21} = 0$, and $\psi_i^\theta = \psi_0^\theta$ $(i = 1, 2, \ldots, m)$.

4.1. Martensitic transformations in a single crystal rectangular plate under tension

We first calculated phase transformations in a rectangular plate, Fig. 4. The boundary conditions on the plate were as follows: $u_n = u_\tau = 0$ along boundary AB; $u_n = v^*t$, $u_\tau = 0$ (v^* is the prescribed normal velocity, t is time and the macrostrain rate $\dot{\varepsilon} = v^*/\text{AD} = 0.5\times10^{-8}\,\text{s}^{-1}$) along boundary CD; and $\sigma = \tau = 0$ (free surface) along boundaries AD and BC. Here u_n and u_τ are the normal and tangential displacements, and τ and σ are the tangential and normal stresses. The MM evolution was calculated to the macrostrain $\varepsilon = v^*t/\text{AD} = 0.1\%$, which was subdivided into 300 load increments. The plate initially consisted of austenite ($c = 0$) with a single martensitic nucleus (one finite element with $c_1 = 1$) in the center of the plate (see Fig. 4). Such a nucleus models heterogeneous nucleation at a strong

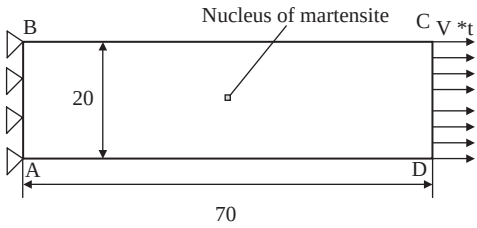

Fig. 4. Cross-section of an austenitic plate with a small initial martensitic nucleus in the middle.

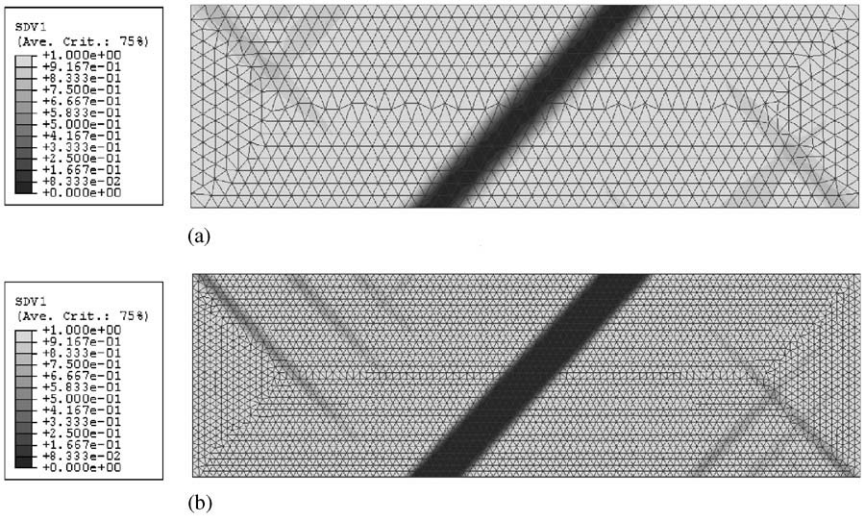

Fig. 5. Distribution of the volume fraction c_1 of the first martensitic variant at the macrostrain $\varepsilon = 0.1\%$ using two different finite element meshes: (a) with 3321 nodes and 1596 six node elements; (b) with 13,487 nodes and 6614 six node elements.

pre-existing defect. Studies of real nucleation must be done at smaller length scales with Landau–Ginzburg models.

The mesh sensitivity of the numerical solution was investigated by using two different finite-element meshes: 3321 nodes (1596 elements) and 13,487 nodes (6614 elements). Fig. 5 shows the distribution of the volume fraction c_1 for variant 1 at the macrostrain $\varepsilon = v^*t/\mathrm{AD} = 0.1\%$ for both meshes. The numerical results are practically mesh independent. Note that the presence of the hardening branch in the stress–strain curve (Figs. 1 and 3) after the softening branch significantly reduces the mesh sensitivity of the solution relative to the case without large-strain hardening, which is used for shear band modeling. For shear banding, the entire shear band region is an instability zone, the width of which is mesh-size sensitive, but

for PT, strain localization is followed by strain delocalization in the hardening branch (similar to that reported in the paper by Beissel and Belytschko (1996) on viscoplastic materials with strain softening). When a martensitic plate is formed, its interior corresponds to the stable hardening branch while the narrow diffuse interface corresponds to the unstable portion of the stress–strain curve. The widths of all diffuse interfaces are controlled by our rate-type regularization rather than by the material parameters. When the loading rate goes to zero and a solution tends to a stationary solution, the rate-type regularization breaks down (as does viscoplastic regularization in plasticity). A stationary solution corresponds to a sharp interface between austenite and martensite. In a numerical solution, however, the minimal interface width is that of a single finite element. During the decrease in the loading rate the interface widths steadily decrease but the change in the thicknesses and orientations of martenasitic plates is small, so the numerical results can be considered mesh insensitive. The mesh independence in our PT model is analogous to that for viscoplastic materials with the stress–strain curve shown in Fig. 1.

We now analyze the morphology and evolution of the microstructure; see Fig. 5. Note first that the second martensitic variant essentially does not appear ($c_2 \approx 0$) during the loading, hence we analyze only the distribution of martensitic variant 1 (Fig. 6). Martensite first appears near the small initial nucleus (due to the favored stress distribution) in the form of two thin orthogonal bands (Fig. 6a–c). Then due to the interaction between these bands one band gradually disappears while the other continues to grow.

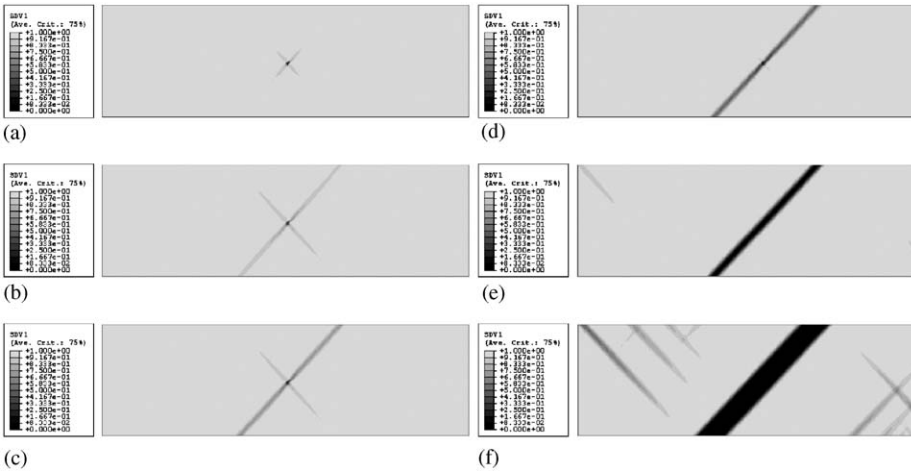

Fig. 6. Evolution of the distribution of the volume fraction c_1 of the first martensitic variant: (a) the macrostrain $\varepsilon = 0.00075\%$; (b) $\varepsilon = 0.003\%$; (c) $\varepsilon = 0.00375\%$; (d) $\varepsilon = 0.0045\%$; (e) $\varepsilon = 0.0075\%$; (f) $\varepsilon = 0.1\%$.

The second band gradually disappears. Thus a reverse PT occurs in some regions under monotonic loading. This phenomenon is quite unexpected and is not predicted by other MM-free micromechanical models (Boyd and Lagoudas, 1996a, b; Hall and Govindjee, 2002; Levitas et al., 1999; Lim and McDowell, 2002). The growth of the initial plate is accompanied by the formation of two new martensitic plates at the corners of the specimen due to stress concentration. Along with the dominant growth of the main plate, new well-spaced plates appear and grow from the free surface (Fig. 6f). All plates are parallel to the invariant plane for ε_{t1}, which is inclined 45°to the tension axis.

The displacement–force diagram, Fig. 7, which is similar to the macroscopic stress–strain curve of the specimen, exhibits a significant drop in macroscopic stress after the onset of the PT. Several additional oscillations in this curve with much smaller magnitudes are caused by the appearance of new plates. Knowledge of such oscillations, which are observed experimentally (Saburi et al., 1986; Krishnan and Brown, 1973), may be important for the design of control systems incorporating shape memory alloys. After some critical strain, the force is nearly constant during further deformation. An increasing σ–ε macroscopic curve, which is observed experimentally, can be modeled by a heterogeneous distribution of k_{10} or A or both. The PT starts at the point with the minimal k_{10} or A; the stress must grow in order for the PT to occur at the points with greater values of k_{10} or A. The parameters k_{10} and A can be determined by comparing experimental and theoretical σ–ε curves under cyclic loading.

The macroscopic properties of materials, in particular, the elastic properties and the macroscopic stress–strain curve, depend on the geometry of the phases. In particular, for significant differences between the elastic properties of the phases (for example, Young's moduli of martensite and austenite in NiTi differ by a factor of 3–4 (Shaw, 2000)) the lower and upper bounds on the effective Young's modulus are quite different. Consequently, our approach gives much more accurate results for the elastic properties and the macroscopic tensor of tangent moduli than those that do not determine the MM (Thamburaja and Anand, 2001; Boyd and Lagoudas, 1996a,

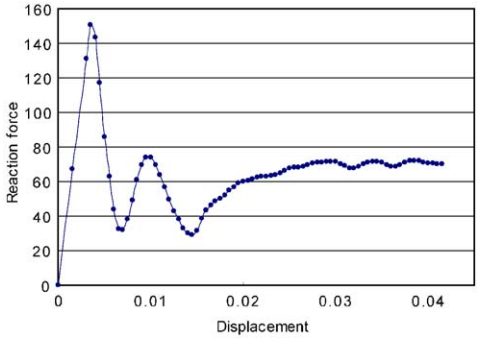

Fig. 7. The displacement–force diagram for the right side (*CD*) of the plate.

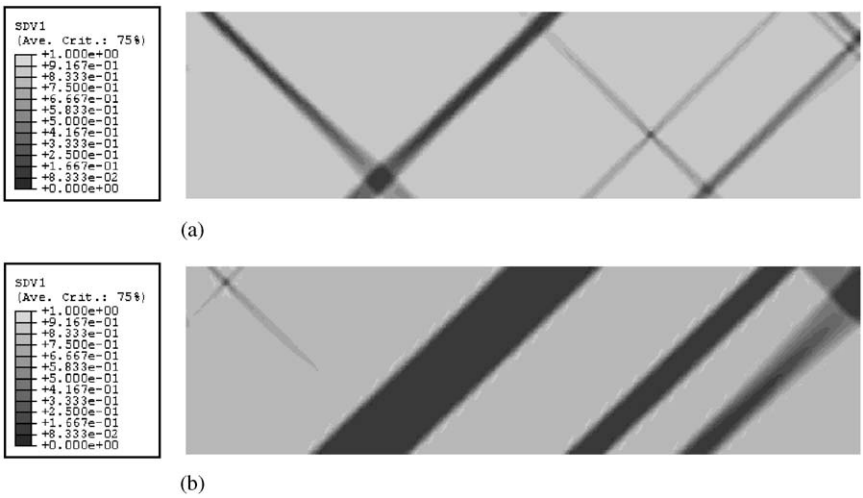

Fig. 8. Distribution of the volume fraction c_1 of the first martensitic variant at the macrostrain $\varepsilon = 0.015\%$ (a) and $\varepsilon = 0.15\%$ (b) for the same boundary conditions as in Fig. 4 but with several initial nuclei distributed randomly in the austenitic plate.

b; Buisson et al., 1991; Govindjee and Miehe, 2001; Hall and Govindjee, 2002; Levitas and Stein, 1997; Levitas et al., 1999; Lim and McDowell, 2002).

Fig. 8 shows the MM for the same problem but with several initial nuclei. Again, one family of parallel martensitic plates suppresses the completely formed ($c \simeq 1$) plates orthogonal to it; here, three plates survive (Fig. 8b). Under further loading (not shown in Fig. 8), the growth of the plate through the corner C (upper right) of the sample is suppressed, while the other two plates grow intensively. When the middle plate approaches the plate passing through C, their interaction causes a slight deviation of the middle plate interface from the invariant plane. It is interesting that simulations resulting in only one family of parallel bands were reported in Beissel and Belytschko (1996) for a 2D plane strain problem with a viscoplastic model.

We next study the effect of varying the relative orientations of the tension axes and the crystal axes of the austenite. In our approach this is equivalent to varying the relative orientations of the tension axes and the transformation strains $\boldsymbol{\varepsilon}_{t1}$ and $\boldsymbol{\varepsilon}_{t2}$. The rotation of the crystal lattice through an angle β about the x_3-axis transforms the components of $\boldsymbol{\varepsilon}_{t1}$ and $\boldsymbol{\varepsilon}_{t2}$ in the global cartesian coordinate system

$$[\varepsilon_{ti}^{\text{new}}] = [\beta]^t [\varepsilon_{ti}][\beta]. \tag{52}$$

Here $[\beta]$ is the rotation matrix about the x_3-axis and $[\varepsilon_{ti}]$ $(i = 1, 2)$ are given by Eqs. (50) and (51). We will consider $\beta = 30^\circ$ and 60°.

Fig. 9 shows the distribution of martensitic variants for different orientations of the transformation strains. As in previous simulations, one martensitic variant prevails during the tensile loading: martensitic variant 1 for the rotation angle $\beta = 30^\circ$ (Fig. 9a) and martensitic variant 2 for the rotation angle $\beta = 60^\circ$ (Fig. 9b). The

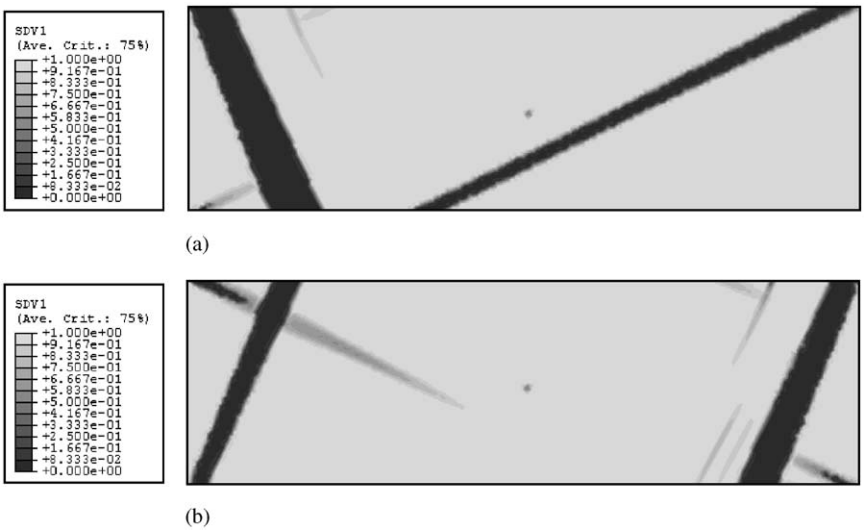

Fig. 9. Distribution of martensitic variants for two orientations of the transformation strains with respect to the tension axes at the macrostrain $\varepsilon = 0.1\%$: (a) martensitic variant 1 for $\beta = 30^\circ$; (b) martensitic variant 2 for $\beta = 60^\circ$.

new martensite appears in bands near the corners of the plate. In both cases the stress concentrations near the corners are more favorable for the formation of new martensite than the region around the small initial nucleus in the center of the plate.

Our 2-D calculations show that martensitic plates are formed parallel to the invariant planes, in agreement with (3-D) experiments. Other 2-D results, namely nucleation in regions of stress concentration or at free surfaces, oscillations in the stress–strain curve, and a strong dependence of microstructure on crystal orientation are similar to the corresponding aspects of the microstructure observed in numerous experiments (Saburi et al., 1986; Krishnan and Brown, 1973; Shield, 1995; Abeyaratne et al., 1996), but detailed comparisons to experiments require the solution of 3-D problems and the introduction of specific heterogeneities (e.g., see Fig. 8).

4.2. *Martensitic transformations in a polycrystalline rectangular plate under tension*

Consider an untextured (random grain orientations) polycrystalline rectangular plate of austenite, Fig. 10. As previously, the PT is constrained to only two martensitic variants. The boundary conditions on the plate were as follows: $u_n = u_\tau = 0$ along boundary AB; $u_n = v^* t$, $u_\tau = 0$ (with the macrostrain rate $\dot{\varepsilon} = v^*/\mathrm{AD} = 0.5 \times 10^{-8}\,\mathrm{s}^{-1}$) along boundary CD; and $\sigma = \tau = 0$ (free surface) along boundaries AD and BC. The total macrostrain $\varepsilon = 0.1\%$ was subdivided into 300 load increments. The plate initially consists of austenite ($c = 0$) with small two nuclei of variant 1 (Fig. 10a). The finite element mesh consisting of 5091 nodes and

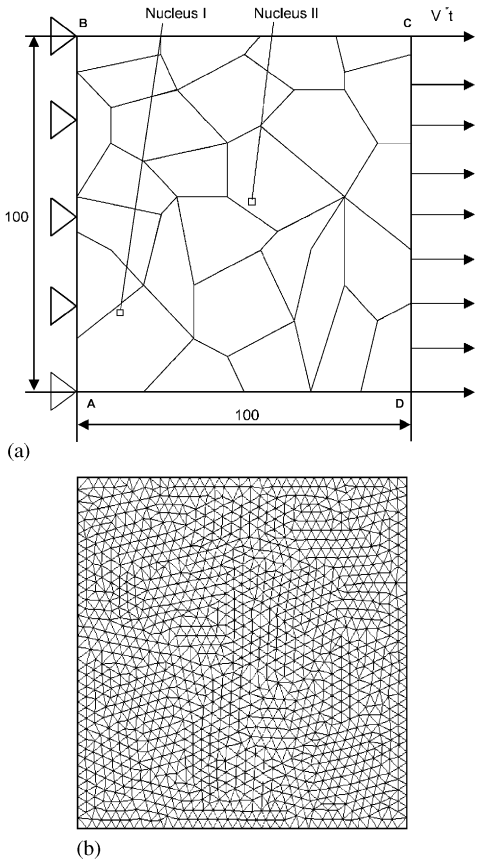

Fig. 10. (a) Cross-section of a polycrystalline austenitic plate with two small initial martensitic nuclei; (b) finite element mesh with 5091 nodes and 2478 six-node finite elements.

2478 six node finite elements is shown in Fig. 10b. The distribution of austenite and two martensitic variants in the plate during tensile loading is given in Fig. 11. During the initial stages of the PT, the growing martensitic plates propagate from one grain to another. Three plates are formed that cross at least half of the specimen, and all are oriented $\simeq 45^{\circ}$ to the tension axis except in one grain where the plate is nearly orthogonal to the load. When the advancing plates cross grain boundaries the martensite can change from one variant to the other depending on the relative grain orientations and internal stress distribution, thus most of the plates consist of both variants. Essentially none of the plates formed during the initial stages of the PT are present in the final calculated state (Fig. 11d). The calculated MM in Fig. 11 is in qualitative agreement with experimentally observed MMs in polycrystals (e.g. see Nishiyama, 1978; McDougall and Wayman, 2003): the MM is comprised of straight, curved, and irregular austenite–martensite interfaces, small regions of residual

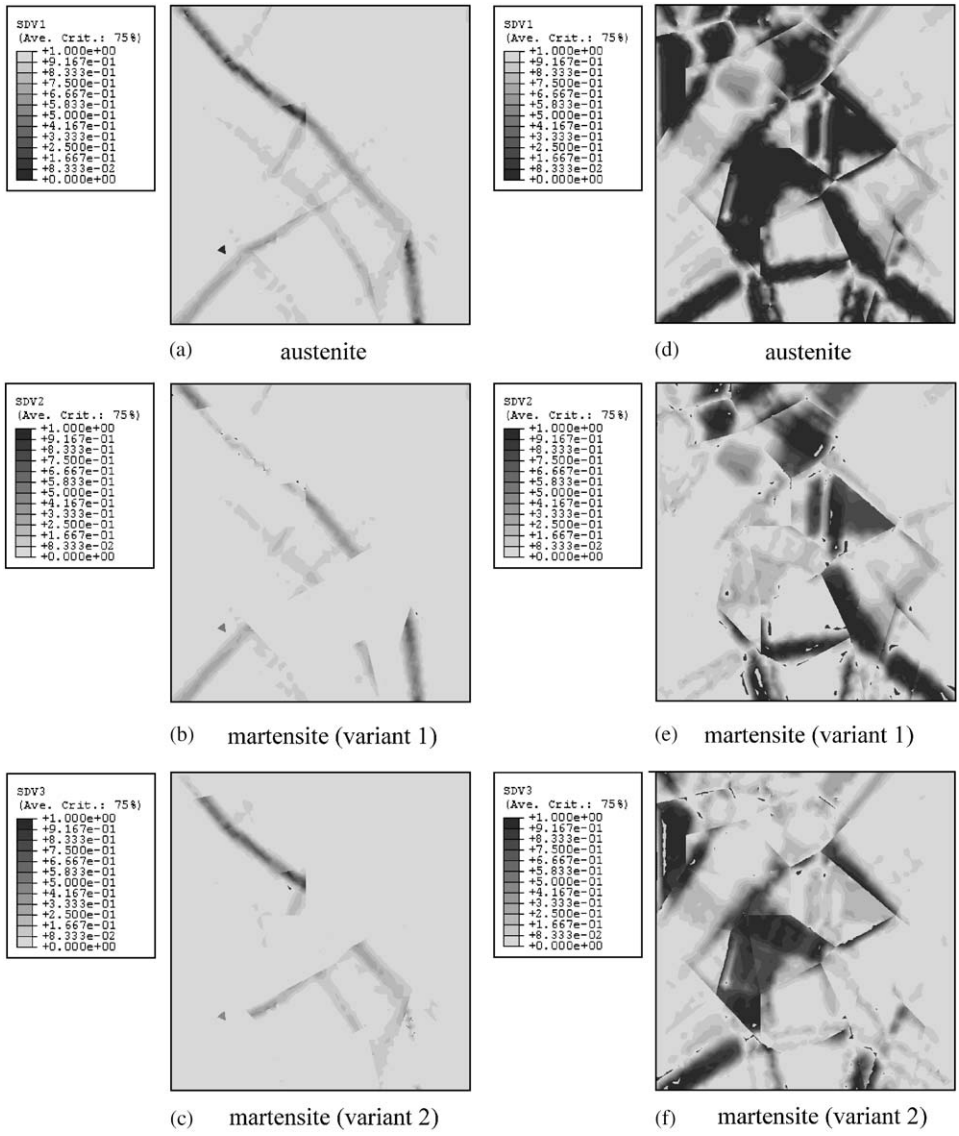

Fig. 11. Distribution of the volume fraction of austenite (white) and mixture of martensitic variants I and II (a,d), the first (b,e) and second (c,f) martensitic variants (black) in the at the macrostrain $\varepsilon = 0.001\%$ (a,b,c) and at the macrostrain $\varepsilon = 0.1\%$ (d,e,f).

austenite locked between martensitic regions, and most of the martensitic regions consist of both variants. The complex coupled evolution of the $\boldsymbol{\sigma}$ and c_i fields results in a complex MM that is neither a global nor a local minimum of the energy because of the dissipative thresholds k_{ij}.

5. Concluding remarks

A new model of multivariant MM formation in elastic materials during temperature- and stress-induced PT was presented. It describes PT in steels, if lattice invariant shear is due to twinning rather than slip, and SMA. In contrast to Ginzburg–Landau models (Artemev et al., 2000, 2001; Saxena et al., 1997; Rasmussen et al., 2001; Wang and Khachaturyan, 1997; Chen and Shen, 1998), our microscale model:

(a) is based on a much larger representative volume element and tracks only the interfaces between austenite and mixtures of the martensitic variants but does not track interfaces between the martensitic variants. The martensite at each point may consist of a mixture of martensitic variants. This is achieved by constructing a microscale Gibbs potential that has minima for pure austenite and martensite but no minima for the individual martensitic variants.

(b) is scale-independent. Nanoscale potentials include a gradient energy term that introduces a length scale, namely, the width of austenite–martensite and martensite–martensite interfaces, which is of order 1 nm. Since there are no interfaces with widths greater than or of order the size of our representative volume, i.e., ~ 100 nm, our microscale model does not include a gradient energy term; the interface energy is taken into account in an averaged sense through the coefficients A^i_{ij}. Consequently, our model has no intrinsic length scale. It can be applied at all scales greater than 100 nm. The kinetic equations for the c_i in our approach are local and much simpler.

(c) accounts for the experimentally observed features of martensitic PT in SMA and steels, specifically, constant (stress-independent) transformation strain tensor and stress hysteresis, and transformation at non-zero elastic moduli, and it can incorporate all temperature-dependent thermomechanical properties of both phases. As shown in Levitas and Preston (2002a, b), Levitas et al. (2003), this is not the case for the nanoscale potentials in Artemev et al. (2000, 2001), Saxena et al. (1997), Rasmussen et al. (2001), Wang and Khachaturyan (1997), and Chen and Shen (1998). The nanoscale potential in Levitas and Preston (2002a, b), and Levitas et al. (2003) incorporates the above features, but it has not yet been used for numerical simulations of MM. It also has a much more complex structure than the microscale potential $G(c_i)$ used in this paper.

(d) includes dissipative thresholds k_{ij}.

Note that our microscale model does not compete with and is not intended to be a substitute for the models in Artemev et al. (2000, 2001), Saxena et al. (1997), Rasmussen et al. (2001), Wang and Khachaturyan (1997), Chen and Shen (1998), Levitas and Preston (2002a, b), and Levitas et al. (2003); they describe the microstructures at different length scales.

Unlike the known microscopic thermomechanical models (Govindjee and Miehe, 2001; Govindjee et al., 2002; Hall and Govindjee, 2002), our microscale model

(a) describes a discrete MM rather than a smeared distribution of austenite and martensite. This is a consequence of $A>0$, A_{ij} small or zero, and removal of the dissipative threshold k_{0i} immediately after "nucleation" of either austenite or a

martensitic variant. Due to internal stresses and the interface energy, the local (microscopic) stress–strain curve (Fig. 1) contains a decreasing unstable branch (strain softening) instead of only strain hardening.

(b) allows a much more accurate determination of the macroscopic mechanical properties of single crystals and polycrystals, in particular, the macroscopic stress–strain curve, since they are sensitive to the microstructure.

In contrast to the thermomechanical models of Thamburaja and Anand (2001), Boyd and Lagoudas (1996a, b), Buisson et al. (1991), Siredey et al. (1999), and Lim and McDowell (2002), our model (in addition to items (a) and (b) above):

(c) is based on Bain strain variants rather than habit plane variants. The habit plane variant is a combination of two Bain strain variants in a specific fixed proportion independent of stress. It is known, however, that the ratio c_1/c_2 varies significantly with the applied stress (Roitburd, 1993; Bhattacharyya and Kohn, 1996). This is neglected in the papers by Thamburaja and Anand (2001), Boyd and Lagoudas (1996a, b), Buisson et al. (1991), Siredey et al. (1999), and Lim and McDowell (2002) but is taken into account in our theory and confirmed in simulations. Also, the number of variants is drastically reduced in our approach, e.g., from 96 habit plane variants to 6 Bain strain variants for the cubic–orthorhombic PT, of which only 2 variants are present at each point; there are 192 habit plane variants for the cubic–monoclinic PT.

(d) is applicable at spatial scales down to 100 nm rather than 1–10 μm because the size of the representative volume element for Bain strain variants is smaller than that for habit plane variants.

In contrast to ersatz models with strain softening (Beissel and Belytschko, 1996; Shaw, 2000), our model is based on the thermomechanics of multivariant martensitic PT. Note that the thermomechanical model of Kuczma et al. (1997) generates a discrete MM, but instead of being a consequence of strain softening it is due to variation of the sample cross-section.

It has been shown that the proposed model can describe the formation of a non-trivial MM during PT. In particular, under monotonic uniaxial loading, some martensitic plates that appear during the initial stages of the PT later disappear, i.e., direct and reverse PTs occur simultaneously. This behavior cannot be obtained in models that neglect the discrete MM. Although intersecting bands of martensite appear during the initial stages of the PT in the single crystal plates, one of the bands invariably disappears, i.e., intersecting martensitic plates are not present in the later stages of the MM evolution. The calculated MM is in qualitative agreement with known experimental MM by Abeyaratne et al. (1996), Shield (1995), Nishiyama (1978), McDougall and Wayman (2003).

From an algorithmic perspective, PT problems in our model are similar to shear band formation problems in viscoplastic material models with strain softening. Rate-dependent constitutive equations suppress mesh sensitivity in the finite element simulations.

We would like to mention that there is nothing wrong with $A<0$ (or $A=0$) in the papers by Thamburaja and Anand (2001), Boyd and Lagoudas (1996a, b), Buisson et al. (1991), Siredey et al. (1999), Lim and McDowell (2002), Govindjee and Miehe

(2001), Govindjee et al. (2002), and Hall and Govindjee (2002) because that is precisely what is needed to describe experimental stress–strain curves with hardening, provided one is not interested in microstructure. For $A>0$, the *local* stress–strain curve cannot be fitted to experiment; hence the change in sign is not trivial. When we derived $A>0$ in our earlier models (Levitas et al., 1998), we assumed a growing dissipative threshold $k(c)$ to obtain hardening only, in agreement with the experimental stress–strain curve.

Our current model with $A>0$ and the corresponding softening branch in the local stress–strain curve does not contradict the experimental result that macroscopic stresses grow or remain constant—the local and macroscopic stress–strain curves are completely different for a material that exhibits strain localization. For fixed values of A and k_{0i}, the macroscopic stress is nearly constant above some critical strain; see Fig. 7. An increasing σ–ε curve, which is observed experimentally, can be realized for a heterogeneous distribution of k_{i0} or A or both. The k_{i0} and A distributions can be obtained by fitting to the measured macroscopic stress–strain curve.

MMs can be realized in the models of Govindjee and Miehe (2001), Hall and Govindjee (2002) by changing the sign of A and removing k. A MM can also be obtained from any model (Thamburaja and Anand, 2001; Boyd and Lagoudas, 1996a, b; Buisson et al., 1991; Levitas and Stein, 1997; Levitas et al., 1999; Lim and McDowell, 2002) if strain softening is included. This makes it possible to model MM at larger spatial scales at the expense of accuracy. If we tolerate the independence of invariant plane strain on the applied stress or take such a dependence into account (for example, as in Levitas and Stein, 1997), our algorithm can be used with habit plane strain instead of Bain strain. However, strain softening can change the type of the system of differential equations, thus the solution is completely different (discrete microstructure vs. smeared distribution of volume fraction), and a number of instability-related computational problems arise.

There are essential differences between martensitic PT in 2-D and 3-D. For example, austenite is geometrically compatible with a single martensitic variant along a specific straight line in 2-D, but austenite is practically never compatible with a single variant in 3-D. This is the main reason for the formation of twinned MM. Also, it is impossible to determine material parameters or quantitatively describe experiments without going to 3-D. However, for complex and non-homogeneous stress fields, as in polycrystals, a single martensitic variant is incompatible with austenite, even in 2-D. The interface is not a straight line (plane); see Fig. 11. As a result, most of the martensitic plates consist of two variants. Also, some martensitic plate boundaries significantly deviate from the invariant plane because of internal stresses and because the ratio c_1/c_2 depends on stress, in contrast to the invariant–plane variant derived in crystallographic theory and used in micromechanical modeling; see Thamburaja and Anand (2001), Boyd and Lagoudas (1996a, b), Buisson et al. (1991), Siredey et al. (1999), and Lim and McDowell (2002). Thus, some typical 3-D features are present in our 2-D simulations. Two-dimensional numerical simulations, which yield a discrete microstructure qualitatively similar to those observed experimentally, are sufficient to demonstrate the utility of our strain softening model for calculating MM evolution. This is not trivial because condition

(25) is only a necessary condition for strain localization; sufficiency of this condition is problem specific and can be proved numerically only. In the future we plan to extend our approach to the solution of 3-D problems. There are no significant obstacles to this generalization, but the computation time increases significantly. Because of instabilities, the computation time will be greater than that required for a smeared description (Thamburaja and Anand, 2001; Boyd and Lagoudas, 1996a, b; Bhattacharya et al., 1997a, b; Buisson et al., 1991; Siredey et al., 1999; Govindjee and Miehe, 2001; Hall and Govindjee, 2002; Levitas and Stein, 1997; Levitas et al., 1999; Lim and McDowell, 2002).

Our model can be extended to encompass plastic materials by including single-crystal viscoplastic constitutive equations. Note that a stress–strain curve of the type shown in Fig. 1 leads to plastic strain localization in macroscopic polycrystalline plasticity theory (Beissel and Belytschko, 1996; Shaw, 2000). Incorporation of such a σ–ε curve for single crystals into our approach would enable us to describe the interaction between plastic and transformational instabilities, in particular PT in shear bands and shear-band intersections, and to determine the conditions for slip or twinning as an accommodation mechanism. The use of such a curve in our macroscopic polycrystalline model for PT (Levitas et al., 1999) would allow us to describe the MM at larger scales, as is observed in experiments on polycrystals (Shaw, 2000).

Acknowledgements

LANL (52844) and TTU support for AVI and VIL, and NSF funding (CMS-02011108) for VIL are gratefully acknowledged.

References

ABAQUS, 2001. Hibbit, Karlsson and Sorensen Inc., ver.6.2.

Abeyaratne, R., Chu, C., James, R., 1996. Kinetics of materials with wiggly energies: theory and application to the evolution of twinning microstructures in a cu-al-ni shape memory alloy. Philos. Mag. A: Phys. Condens. Matter Struct., Defects Mech. Properties 73 (2), 457–497.

Artemev, A., Wang, Y., Khachaturyan, A., 2000. Three-dimensional phase field model and simulation of martensitic transformation in multilayer systems under applied stresses. Acta Mater. 48 (10), 2503–2518.

Artemev, A., Jin, Y., Khachaturyan, A., 2001. Three-dimensional phase field model of proper martensitic transformation. Acta Mater. 49 (7), 1165–1177.

Bathe, K., 1996. Finite Element Procedures. Prentice-Hall, Upper Saddle River, NJ.

Beissel, S., Belytschko, T., 1996. On patterns of deformation in phase transformations and luders bands. Int. J. Solids Struct. 33 (12), 1689.

Bhattacharyya, K., Kohn, R.V., 1996. Symmetry, texture and the recoverable strain of shape-memory polycrystals. Acta Mater. 4, 529–542.

Bhattacharya, K., James, R., Swart, P., 1997a. Relaxation in shape-memory alloys—Part I. mechanical model. Acta Mater. 45 (11), 4547–4560.

Bhattacharya, K., James, R., Swart, P., 1997b. Relaxation in shape-memory alloys—Part II. thermo-mechanical model and proposed experiments. Acta Mater. 45 (11), 4561–4568.

Boyd, J.G., Lagoudas, D.C., 1996a. Thermodynamical constitutive model for shape memory materials. Part I. The monolithic shape memory alloy. Int. J. Plasticity 12 (6), 805–842.

Boyd, J.G., Lagoudas, D.C., 1996b. Thermodynamical constitutive model for shape memory materials. Part II. The SMA composite material. Int. J. Plasticity 12 (7), 843–873.

Buisson, M., Patoor, E., Berveiller, M., 1991. Constitutive equations for deformations induced by interfacial motions. In: Proceedings of PLASTICITY '91: The Third International Symposium on Plasticity and Its Current Applications. Elsevier Science Publ Ltd., Barking, UK, Paris, France, p. 536.

Chen, L., Shen, J., 1998. Applications of semi-implicit Fourier-spectral method to phase field equations. Comput. Phys. Commun. 108 (2–3), 147–158.

Govindjee, S., Miehe, C., 2001. A multi-variant martensitic phase transformation model: formulation and numerical implementation. Comput. Methods Appl. Mech. Eng. 191 (3–5), 215–238.

Govindjee, S., Mielke, A., Hall, G.J., 2002. Polycrystalline shape-memory materials: effect of crystallographic texture. J. Mech. Phys. Solids 51 (4), I–XXVI.

Hall, G.J., Govindjee, S., 2002. Application of a partially relaxed shape memory free energy function to estimate the phase diagram and predict global microstructure evolution. J. Mech. Phys. of Solids 50 (3), 501–530.

Huo, Y., Mueller, I., 1993. Thermodynamics of pseudoelasticity—a graphical approach. Continuum Mech. Thermodyn. 5, 163–204.

Kohn, R., 1991. The relaxation of a double-well energy. Continuum Mech. Thermodyn. 3, 193–236.

Krishnan, R.V., Brown, L., 1973. Pseudoelsticity and strain-memory effect in an ag-45 at. pct. cd alloys. Metall. Trans. 4 (2), 423–429.

Kuczma, M., Levitas, V., Mielke, A.E.S., 1997. Nonisothermal hysteresis loops in pseudoelasticity. In: Proceedings of the XIII Conference on Computer Methods in Mechanics, Posnan, 5–8 May 1997, pp. 711–718.

Levitas, V., Preston, D., 2002a. Three-dimensional landau theory for multivariant stress-induced martensitic phase transformations. Part I. austenite ↔ martensite. Phys. Rev. B 66, 134206 (1–9).

Levitas, V., Preston, D., 2002b. Three-dimensional landau theory for multivariant stress-induced martensitic phase transformations. Part II. multivariant phase transformations and stress space analysis. Phys. Rev. B 66, 134207 (1–15).

Levitas, V., Idesman, A., Stein, E., Spielfeld, J., Hornbogen, E., 1998. Simple micromechanical model for pseudoelastic behavior of *cuznal* alloy. Int. J. Intelligent Mater. Systems Struct. 9 (5), 324–334.

Levitas, V., Idesman, A., Stein, E., 1999. Shape memory alloys: micromechanical modeling and numerical analysis of structures. Int. J. Intelligent Mater. Systems Struct. 10 (12), 983–996.

Levitas, V., Preston, D., Lee, D.-W., 2003. Three-dimensional landau theory for multivariant stress-induced martensitic phase transformations. Part III. alternative potentials, critical nuclei, kink solutions, and dislocation theory. Phys. Rev. B 68, 134201.

Levitas, V.I., Stein, E., 1997. Simple micromechanical model of thermoelastic martensitic transformations. Mech. Res. Commun. 24 (3), 309–318.

Levitas, V.I., Idesman, A.V., Preston, D.L., 2004. Microscale simulation of evolution of martensitic microstructure. Phys. Rev. Lett. 93 (10), 105701.

Lim, T., McDowell, D.L., 2002. Cyclic thermomechanical behavior of a polycrystalline pseudoelastic shape memory alloy. J. Mech. Phys. Solids 50 (3), 651–676.

McDougall, P., Wayman, C., 2003. The crystallography and morphology of ferrous martensites. In: Olson, G.B., Owen, W.S. (Eds.), Martensite. CBLS, p. 59.

Needleman, A., 1988. Material rate dependence and mesh sensitivity in localization problems. Comput. Methods Appl. Mech. Eng. 67 (1), 69–85.

Nishiyama, Z., 1978. Martensitic Transformation. Academic Press, New York.

Olson, G., 1997. Computational design of hierarchically structured materials. Science 277 (5330), 1237–1242.

Olson, G.B., Cohen, M., 1986. Dislocation theory of martensitic transformations. In: Nabarro, F.R.N. (Ed.), Dislocations in Solids. Elsevier Science Publishers, Amsterdam, pp. 297–407.

Ortiz, M., Repetto, E.A., 1999. Nonconvex energy minimization and dislocation structures in ductile single crystals. J. Mech. Phys. Solids 47 (2), 397–462.

Pitteri, M., Zanzotto, G., 2003. Continuum Models for Phase Transformations and Twinning in Crystals. Hall/CRC, Boca Raton, London, New York.

Rasmussen, K., Lookman, T., Saxena, A., Bishop, A.R., Albers, R.C., Shenoy, S.R., 2001. Three-dimensional elastic compatibility and varieties of twins in martensites. Phys. Rev. Lett. 87, 055704.

Roitburd, A.L., 1993. Elastic domains and polydomain phases in solids. Phase Transit. 45, 1–33.

Saburi, T., Nenno, S., Nishimoto, Y., Zeniya, M., 1986. Effects of thermomechanical treatment on the shape memory effect and the pseudoelasticity of ti-50.2ni and ti-47.5ni-2.5fe alloys. Tetsu to Hagane—J. Iron Steel Inst. Jpn. 72 (6), 571–578.

Saxena, A., Wu, Y., Lookman, T., Shenoy, S., Bishop, A., 1997. Hierarchical pattern formation in elastic materials. Physica A: Stat. Theoret. Phys. 239 (1–3), 18–34.

Shaw, J.A., 2000. Simulations of localized thermo-mechanical behavior in a niti shape memory alloy. Int. J. Plasticity 16 (5), 541–562.

Shield, T., 1995. Orientation dependence of the pseudoelastic behavior of single crystals of cu-al-ni in tension. J. Mech. Phys. Solids 43 (6), 869–895.

Simo, J., Hughes, T., 1998. Computational Inelasticity. Springer, New York.

Siredey, N., Patoor, E., Berveiller, M., Eberhardt, A., 1999. Constitutive equations for polycrystalline thermoelastic shape memory alloys. Part I. Intragranular interactions and behavior of the grain. Int. J. Solids Struct. 36 (28), 4289–4315.

Thamburaja, P., Anand, L., 2001. Polycrystalline shape-memory materials: effect of crystallographic texture. J. Mech. Phys. Solids 49 (4).

Truskinovsky, L., 1994. About the normal growth approximation in the dynamical theory of phase-transitions. Continuum Mech. Thermodyn. 6 (3), 185–208.

Wang, Y., Khachaturyan, A., 1997. Three-dimensional field model and computer modeling of martensitic transformations. Acta Mater. 45 (2), 759–773.